International Journal on Magnetic Particle Imaging
Vol 5, No 1-2, Article ID 1908001, 7 Pages

Infinite Science Publishing

Research Article

Temporal Polyrigid Registration for Patch-based MPI Reconstruction of Moving Objects

Jan Ehrhardt[a,*] · Mandy Ahlborg[b] · Hristina Uzunova[a] · Thorsten M. Buzug[b] · Heinz Handels[a]

[a]Institute of Medical Informatics, Universität zu Lübeck, Lübeck, Germany
[b]Institute of Medical Engineering, Universität zu Lübeck, Lübeck, Germany
[*]Corresponding author, email: ehrhardt@imi.uni-luebeck.de

Received 02 May 2019; Accepted 19 July 2019; Published online 23 August 2019

Abstract

In Magnetic Particle Imaging, the size of the field of view can be increased with static focus fields resulting in imaging patches. Patches are acquired successively and combined during or after image reconstruction. However, the occurrence of motion may result in artifacts in the reconstructed images. In this contribution, a temporal polyrigid registration is proposed to combine reconstructed MPI patches by predicting a possible object motion. The experiments use different two-dimensional simulated MPI acquisition scenarios. It is shown that our approach reduces motion artifacts in dependence of the used patch overlaps successfully.

I. Introduction

The imaging technology Magnetic Particle Imaging (MPI) allows the detection of superparamagnetic nanoparticles [1]. One possible application of this technique is *in vivo* medical imaging, where the particles are e.g. applied as tracer directly into the blood stream and allow the diagnosis of a series of medical questions [2]. In MPI, magnetic fields called drive fields are used to remagnetize the nanoparticles. Consequentially, a signal is induced in dedicated receive coils. A gradient field featuring a field free point (FFP) is used to spatially encode the area where particles contribute to this signal. Additionally, the drive fields are used to shift the FFP through a certain field of view (FOV) whose size is limited. One of the main reasons for this restriction is the planned use on living individuals, because potential tissue heating or stimulation of nerves limit the applicable field amplitudes [3]. A possible approach to cope with this problem is a patch-wise acquisition of the required region of interest (ROI). This technique uses a successive measurement of several FOVs with varying positions to cover the entire ROI [4, 5]. The patches can be acquired in an overlapping manner in order to use redundant information for the reduction of truncation artifacts [6]. Because the relative position of the acquired patches is known, the reconstruction of the ROI is straight-forward for static objects. However, the application on living organisms [7] implies the occurrence of motion during image acquisition, and therefore a patch-wise reconstruction has to account for object motion during the acquisition process. Figure 1 (right) visualizes the influence of object motion on a reconstructed image. Composing an image from multiple patches is a known problem in image processing and referred to as mosaicking or stitching [8]. Classic algorithms account for camera movement between patches acquired successively, and have e.g. medical applications in endoscopic imaging [9]. The compensation of object

Figure 1: Simulated MPI images: software phantom (left), simulated image without object motion (center), and with circular object motion for $\alpha = 5$ (right).

motion in a static acquisition system has applications in tomographic imaging, like computed tomography (CT) and magnetic resonance imaging (MRI). One approach to compensate periodic motions uses a binning and averaging technique [10], and was recently adapted for MPI acquisitions [11]. Here, repeated acquisitions of the ROI are performed and signals detected at the same state of the periodic motion are combined to form an average signal for this motion state. This was also applied to a patch-wise acquisition of MPI images [12]. Another class of approaches use image registration for motion compensation during the image reconstruction [13–15]. Here, image intensities and object motion are estimated during the reconstruction. The advantage of these methods is that they are not limited to periodic motion and information of several motion phases can be considered to reconstruct the image.

In this work, we follow a patch-wise and registration-based approach. We use reconstructed image patches to predict the underlying object motion and to generate a "plausible" image of the entire ROI. Registration has previously been used for improved reconstruction of 4D CT or 4D MRI images in two steps: the object motion is first estimated and then used to generate improved images [13, 15]. In contrast, this work uses an integrated approach, i.e. image and object motion are estimated simultaneously. Compared to [11, 12] we do not assume periodic motion and repeated acquisitions. Instead, we assume a rigid object motion that can be considered approximately correct if the measured ROI is relatively small compared to the organ size. However, the approach presented can also be extended to non-rigid motions.

II. Methods and Material

II.I. Temporal Polyrigid Registration

Given N overlapping patches of image regions $\Omega_i \subset \mathbb{R}^d$, $i = 1,...,N$ with acquired particle concentrations c_i at time points $\tau_i \in [0, T]$, we aim to find the particle concentration $c : \Omega \to \mathbb{R}$ in the entire ROI $\Omega = \bigcup_{i=1}^{N} \Omega_i$ and the associated spatial-temporal object motion $\boldsymbol{\phi} : \Omega \times [0, T] \to \Omega$ during acquisition.

II.I.1. Transformation Model

The spatial-temporal motion $\boldsymbol{\phi}$ is assumed to describe a rigid body motion, i.e. for a fixed time point $\hat{\tau}$ the transformation is an element of the special Euclidean group $\boldsymbol{\phi}(\cdot, \hat{\tau}) \in \mathrm{SE}(d)$ and $\boldsymbol{\phi}(\boldsymbol{x}, \tau)$ is smooth in spatial and temporal direction. We parameterize the object motion with a small number of rigid key-point transformations $A_1, \ldots, A_K$ given as matrices in homogeneous coordinates. In the following and throughout this manuscript all spatial coordinates are given in homogeneous coordinates $\boldsymbol{x} \in \mathbb{R}^{d'}$ with $d' = (d+1)$. Further, each key-point transformation is associated with a non-negative smooth weighting function $w_k : [0, T] \to \mathbb{R}_+$ subject to the condition $\sum_{k=1}^{K} w_k(\tau) = 1, \forall \tau \in [0, T]$. Note, that averaging the key-point transformations to compute $\boldsymbol{\phi}$ at a given time-point by $\boldsymbol{\phi}(\boldsymbol{x}, \hat{\tau}) = \sum_k w_k(\hat{\tau}) A_k \boldsymbol{x}$ results in non-rigid transformations and can not ensure temporal smoothness constraints, among other disadvantages [16].

To ensure our motion assumptions, the transformation is parameterized using the Log-Euclidean framework [16]. Log-Euclidean polyaffine registration was introduced to fuse spatially local affine transformations into a global diffeomorphism using weight functions [16]. We adapt this concept for the time-varying polyrigid registration of image patches and compute the transformation $\boldsymbol{\phi}$ as the weighted *log-Euclidean mean* of the key-point transformations:

$$\boldsymbol{\phi}(\boldsymbol{x}, \tau) = \exp\left(\sum_{k=1}^{K} w_k(\tau) M_k\right) \boldsymbol{x}, \tag{1}$$

where M_k is the matrix logarithm $M_k = \log(A_k)$ of the rigid key-point transformation given in homogeneous coordinates. Matrix logarithm and matrix exponential in (1) may e.g. be computed using the (inverse) scaling-and-squaring method [16, 17].

Note, that the resulting transformation $\boldsymbol{\phi}(\boldsymbol{x}, \tau)$ is a rigid transformation for any τ and a diffeomorphism, i.e. C^∞ with respect to spatial position and time with an inverse given by $\boldsymbol{\phi}^{-1}(\cdot, \tau) = \exp\left(-\sum_{k=1}^{K} w_k(\tau) M_k\right)$. A common choice is to use Gaussian weighting functions:

$$w_k(\tau) = \frac{1}{Z} e^{-\frac{|\tau - t_k|^2}{\sigma_\tau^2}}, \text{ with } Z = \sum_{k=1}^{K} e^{-\frac{|\tau - t_k|^2}{\sigma_\tau^2}}, \tag{2}$$

where $t_1, \ldots, t_K$ are the anchor times of the key-point transformations and σ_τ^2 defines the size of the influence intervals.

II.I.2. Registration Algorithm

To estimate the particle concentration c and underlying object motion from the acquired image patches we use a pair-and-smooth approach [18] that introduces auxiliary

10.18416/ijmpi.2019.1908001

variables φ_i and can be formulated as:

$$\mathcal{J}(c,\boldsymbol{\phi},\varphi_1,\ldots,\varphi_N)=\sum_{i=1}^{N}\int_{\Omega_i}\left\|c\left(\varphi_i(\boldsymbol{x})\right)-c_i\left(\boldsymbol{x}\right)\right\|^2\,d\boldsymbol{x} + \eta\sum_{i=1}^{N}\operatorname{dist}\left(\boldsymbol{\phi}(\cdot,\tau_i),\varphi_i\right)+\beta\mathfrak{R}(\boldsymbol{\phi}). \quad (3)$$

The first term measures the (dis-)similarity between each acquired image patch and the global particle concentration given the patch-specific transformations φ_i. The second term projects the patch-specific transformations φ_i onto the temporal transformation model. The log-Euclidean framework is used to define distances between transformations by

$$\begin{aligned}\operatorname{dist}\left(\boldsymbol{\phi}(\cdot,\tau_i),\varphi_i\right)&=\|\log\boldsymbol{\phi}(\cdot,\tau_i)-\log\varphi_i\|_F^2\\&=\left\|\sum_{k=1}^{K}w_k(\tau_i)M_k-\log\varphi_i\right\|_F^2,\end{aligned} \quad (4)$$

where $\|\cdot\|_F$ is the Frobenius matrix norm.

The third term is used to add further regularization constraints on the transformation, e.g. to control the similarity of temporally neighboring rigid matrices by

$$\mathfrak{R}(\boldsymbol{\phi})=\sum_{k=1}^{K}\sum_{j=1}^{K}\pi_{jk}\|M_j-M_k\|_F^2 \quad (5)$$

$$\text{with}\quad \pi_{jk}=\int_0^T w_j(\tau)w_k(\tau)d\tau. \quad (6)$$

In contrast to the direct optimization of key-point transformations by a gradient descent approach previously proposed in [19], the pair-and-smooth formulation of the problem simplifies the optimization and adds flexibility to the algorithms.

II.1.3. Implementation Details

(3) is minimized using an alternating optimization with respect to c, φ_i, and $\boldsymbol{\phi}$. The interest of introducing auxiliary variables φ_i is that an alternating optimization decouples the complex minimization into simple and very efficient steps.

The optimization process is initialized by identity key-point transformations $A_1,\ldots,A_K=I_{d'\times d'}$ resulting in zero logarithm matrices $M_1,\ldots,M_K=\mathbf{0}_{d'\times d'}$. The initial transform $\boldsymbol{\phi}$ is computed by (1) with temporal weighting functions according to (2).

Given the current spatial-temporal transformation $\boldsymbol{\phi}$ the combined particle concentration is computed by

$$c(\boldsymbol{x})=\sum_{i=1}^{N}\gamma_i\left(\boldsymbol{x}_i'\right)c_i\left(\boldsymbol{x}_i'\right)\quad\text{with } \boldsymbol{x}_i'=\boldsymbol{\phi}^{-1}(\boldsymbol{x},\tau_i), \quad (7)$$

where $\boldsymbol{x}_i'$ is the corresponding position of $\boldsymbol{x}$ for the i-th patch, i.e. at acquisition time τ_i. The spatial weighting functions $\gamma_i:\Omega\to[0,1]$ are non-zero only inside the patch regions $\forall\boldsymbol{x}\notin\Omega_i:\gamma_i(\boldsymbol{x})=0$. To reduce the influence of truncation artifacts at patch borders, a linear weighting scheme in patch-overlap regions is applied [6]. Here, the intensity information of overlapping pixels is combined using weights linearly depending on the distance to the respective patch border.

Each patch-specific motion φ_i can be updated independently using a standard rigid registration approach, e.g. by solving

$$\begin{aligned}&\min_{\varphi_i}\int_{\Omega_i}\left\|\tilde{c}\circ\left(\varphi_i(\boldsymbol{x})\right)-c_i\left(\boldsymbol{x}\right)\right\|^2\,d\boldsymbol{x}\\&\quad+\eta\|\log\boldsymbol{\phi}(\cdot,\tau_i)-\log\varphi_i\|_F^2\end{aligned} \quad (8)$$

using gradient descent. This type of partial data registration, however, presents difficulties and we follow the steps below to speed-up and stabilize the optimization process. First, in each iteration the current motion estimate is used for initialization $\varphi_i=\boldsymbol{\phi}^{-1}(\cdot,\tau_i)$. Further, we use patch-specific reconstructions in the registration step, i.e. for computing the transformation φ_i of the i-th patch, the particle concentration c_i is not used to generate the total particle concentration to be registered with

$$\tilde{c}(\boldsymbol{x})=\sum_{j\neq i}\gamma_j\left(\boldsymbol{x}_j'\right)c_j\left(\boldsymbol{x}_j'\right). \quad (9)$$

A mask restricts the registration procedure to valid regions fulfilling $\sum_{j\neq i}\gamma_j(\boldsymbol{x}_j')>0$.

The computed patch-specific transformations $\varphi_1,\ldots,\varphi_N$ are projected onto the space of temporal polyrigid transformations by the minimization of

$$\min_{M_1,\ldots,M_K}\sum_i\left\|\log\varphi_i-\sum_k w_k(\tau_i)M_k\right\|_F^2+\lambda\mathfrak{R}(M), \quad (10)$$

with $\lambda=\frac{\beta}{\eta}$ and $\mathfrak{R}(M)$ according to (5). (10) is minimized by solving the linear equation system

$$M=B(\Gamma+\lambda R)^{-1} \quad (11)$$

for $M=[M_1,\ldots,M_K]^T$. The matrix B is composed of K submatrices $B_k=\sum_{i=1}^{N}w_k(\tau_i)\log\varphi_i$. Γ and R arise from the projection term and the regularizer and are given by $\Gamma=\tilde{\Gamma}\otimes I_{d'\times d'}$ and $R=\tilde{R}\otimes Q$ with

$$\left(\tilde{\Gamma}\right)_{jk}=\pi_{jk}\quad(\text{see }(6)) \quad (12)$$

$$\left(\tilde{R}\right)_{jk}=\begin{cases}-\pi_{jk} & \text{for } j\neq k\\ \sum_{j\neq k'}\pi_{jk'} & \text{for } j=k\end{cases}. \quad (13)$$

The matrix $Q=\operatorname{diag}(1,\ldots,1,s)\in\mathbb{R}^{d'\times d'}$ allows to account for the different scaling between the rotation part of the rigid transformation matrix and the translation part, e.g. by choosing $s=100$. See [20] and [21] for a detailed derivation of these matrices. The pseudo inverse $(\Gamma+\lambda R)^{-1}$ can be precomputed to solve (11) efficiently in each iteration. The patch-based temporal polyrigid registration algorithm is summarized in Algorithm 1.

The set of representable motion trajectories $\boldsymbol{\phi}$ is determined by the weighting functions w_k, the number of key-point transformations K, and the regularization factor λ. As can be seen from (6), (12), and (13), condition and well-posedness of equation system (11) essentially depends on the choice of the weighting functions w_k. For non-overlapping weighting functions,(11) decomposes into K independent systems and the regularization term no longer has any influence. In contrast, constant weighting functions $w_k(\tau) = \frac{1}{K}$ and $\lambda \approx 0$ result in a highly ill-posed problem. Further, K can be chosen independent of N, however, for $K \geq N$ and $\lambda = 0$ no regularity is added, i.e. $\boldsymbol{\phi}(\cdot, \tau_i) = \varphi_i$. There is an ongoing debate how to select the number of key-points and weighting functions w_k in poly-rigid/poly-affine registration. The proposed solutions include to use anatomical constraints [21] or to estimate the parameters K, σ_τ^2, and $t_1, \ldots, t_k$ during the optimization process [22, 23]. A more pragmatic solution is to select equidistant anchor points $t_1, \ldots, t_k$ and choose σ_τ^2 in (2) to ensure a smooth transition between key-point transformations.

Algorithm 1 Patch-based temporal polyrigid registration

Input: patch-wise particle concentrations $c_1, \ldots, c_N$
Output: total particle concentration c,
motion trajectory $\boldsymbol{\phi}(\boldsymbol{x}, \tau)$
initialize key-point transformations with identity
$M_1, \ldots, M_K = \mathbf{0}_{d' \times d'}$
Compute temporal weighting functions w_k by (2)
Compute spatial weight masks $\gamma_i, i = 1, \ldots, N$
Precompute matrices Γ and R (see (12)–(13))
Precompute pseudo inverse $(\Gamma + \lambda R)^{-1}$ using SVD
//Outer loop (projection onto polyrigid transform)
while not converged **do**
Compute current transformations
$\boldsymbol{\phi}(\cdot, \tau_i) = \exp\left(\sum_k w_k(\tau_i) M_k\right), \ (i = 1, \ldots, N)$
//Inner loop (patch-wise registrations)
for $i = 1, \ldots, N$ **do**
Compute current particle concentration $\tilde{c}$
without patch c_i using (9)
Compute transformation φ_i:
rigid registration of $\tilde{c}$ and patch c_i
initialize registration with $\varphi_i = \boldsymbol{\phi}(\cdot, \tau_i)$
end for
Compute Matrix B
Compute $M_1, \ldots, M_K$ using (11)
end while
Compute final transformation $\boldsymbol{\phi}$ using (1)
Compute final particle concentration c by (7)

II.II. Simulated MPI Data

For a first evaluation of the proposed approach a simulation study is performed using different motion patterns, patch-overlaps, and registration parameters.

The MPI simulation assumes an homogeneous drive field with varying size (depending on the patch size), a linear selection field of 2.5 T m^{-1}, and a particle magnetization based on the Langevin theory of paramagnetism, i.e. no relaxation effects are considered.

The ROI is divided into nine patches. A constant pixel spacing of 0.25 mm is used in all experiments and the patch centers are kept constant while the patch FOVs are varied to generate different patch overlaps. Therefore, the size of the ROI depends on the patch overlap and is 32.5×32.5 mm^2 for FOVs of 12.5×12.5 mm^2 (50×50 pixels) and a patch overlap of 2.5 mm (10 pixels).

The simulation study uses the software phantom shown in Figure 1 (left), which mimics a vessel tree. The phantom size is chosen according to the size of the ROI and a normalized period length of $T = 1$ and equidistant patch acquisition times τ_i are assumed in all experiments. Two different motion patterns with amplitudes α are investigated: respiration-related motion in y-direction [24] and a circular object motion:

$$\boldsymbol{\phi}_1(\boldsymbol{x}, \tau) = \begin{pmatrix} x \\ y \end{pmatrix} + \begin{pmatrix} 0 \\ \alpha \begin{cases} 1 - \cos\left(\frac{5}{2}\pi\tau\right) & 0 \leq \tau < 0.4 \\ 1 - \cos\left(\frac{5}{3}\pi(1-\tau)\right) & 0.4 \leq \tau < 1 \end{cases} \end{pmatrix} \tag{14}$$

$$\boldsymbol{\phi}_2(\boldsymbol{x}, \tau) = \begin{pmatrix} x \\ y \end{pmatrix} + \begin{pmatrix} \alpha \sin(2\pi\tau) \\ \alpha \cos(2\pi\tau) \end{pmatrix}. \tag{15}$$

Simulated MPI images without motion ($\alpha = 0$) and with circular object motion ((15), $\alpha = 5$) are shown in Figure 1. Motion artifacts are clearly visible in the right image. Note the presence of truncation artifacts at the patch borders.

III. Results

III.I. Parameter Identification

The first experiment investigates the influence of the parameters of the registration algorithm. Therefore, nine patches of 60 × 60 pixels using 20 pixels overlap are generated to image the ROI during a simulated respiration-like motion ($\alpha = 5$). We use equidistant anchor points $t_1, \ldots, t_K$ and analyze different combinations of the parameters K, σ_τ^2, and λ by comparing computed transformations to the known ground truth motion. Our results show a good fit of the motion curves for a wide range of parameter combinations, as long as $K \geq 5$. The most prominent influence showed the regularization parameter λ, so a good parameter selection strategy is to choose reasonable values K and σ_τ^2 and to tune the parameter λ.

10.18416/ijmpi.2019.1908001

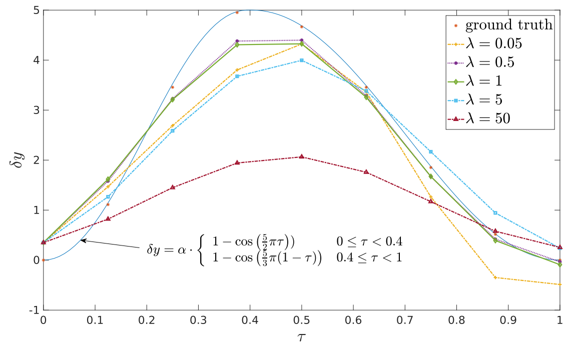

Figure 2: Motion curve for respiration-related motion (14) and recovered motion for different regularization parameters λ.

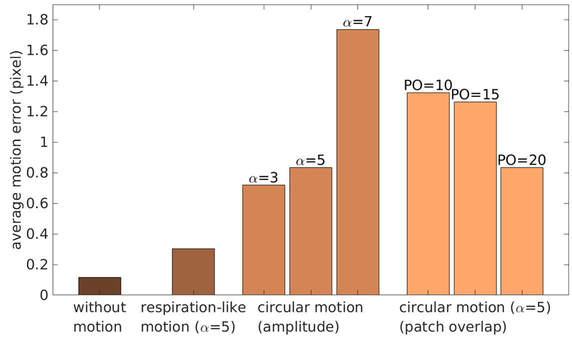

Figure 3: Average registration error in pixels for different motion patterns, motion amplitudes, and patch overlaps (PO).

We chose $\sigma_\tau^2 = \frac{2T}{K+1}$ to ensure smooth motion curves and well-posedness of (11). Selecting $K = N(=9)$ allows arbitrary motion curves and causes the regularization to be controlled via λ alone. Figure 2 shows the influence of λ for respiration-like object motion. As expected, high values increase the temporal smoothness but progressively hinder the adaptation to the real motion. Conversely, low values of λ impede the correct registration of patches with little structural information. Parameter settings $K = 9, \sigma_\tau^2 = 0.2$, and $\lambda = 1$ are used in all following experiments. The remaining parameter η depends on the intensity value range and the noise level of the input images. Large values increase the total computation time, while at low values the algorithm may get stuck in a local minimum.

III.II. Image Reconstruction Results

The next experiments investigate the influence of motion amplitude and motion pattern. Again, nine patches are used to image the ROI, but different types of object motion were simulated during the acquisition: no motion, respiration-like motion ($\alpha = 5$), and circular motion ($\alpha \in \{3,5,7\}$). For these data, the correct motion $\boldsymbol{\phi}^\star$ is known, and we can determine the average pixel-wise registration error for the calculated motion by $\bar{e} = \frac{1}{N}\sum_{i=1}^{N}\frac{1}{|\Omega_i|}\sum_{\boldsymbol{x}\in\Omega_i}\left\|\boldsymbol{\phi}^\star(\boldsymbol{x},\tau_i)-\boldsymbol{\phi}(\boldsymbol{x},\tau_i)\right\|_2$.

Figure 3 shows average registration errors (in pixels). Registration errors increase with motion amplitudes, but for moderate motion an average registration error below one pixel is possible. Further, Figure 3 shows that larger patch overlaps increase registration accuracy by comparing the influence of different patch overlaps. Note that the maximum motion difference between neighboring patches is 9.3 pixels for circular motion with $\alpha = 5$ and 12.9 pixels with $\alpha = 7$ in our setting. An overlap of 10 pixels means that there is no common image information between some adjacent patches, i.e. a registration would not be possible without the temporal smoothness constraint. Despite that fact, an average registration error of less than 1.5 pixels can be achieved with our approach.

Figure 4 shows some results of our simulation experiments including the worst case result for circular motion with a large amplitude of $\alpha = 7$. Reconstruction without motion compensation results in duplicated or blurred structures and discontinuities at the patch borders. In contrast, our approach results in distinct structures and continuous transitions between patches. Relatively high registration errors occur for the lower three patches caused by the low textural information and the high ratio of motion to patch overlap. The precomputation of the projection matrix $(\Gamma + \lambda R)^{-1}$ allows an efficient motion compensation with run-times below 20 s for the simulated 2D images using a non-optimized single-core implementation.

IV. Conclusion

In this paper, we addressed the necessity to account for object motion when a patch-wise acquisition of MPI data on living individuals is desired. To solve this problem, we proposed a registration-based method to reconstruct a motion-compensated image of the ROI from the acquired image patches. Our approach relies on a polyrigid transformation model of the underlying object motion that ensures temporal smoothness and is crucial for the robustness of the presented method. We derived an optimization criterion for the simultaneous estimation of reconstructed image and underlying object motion that can be efficiently solved using an alternating optimization scheme.

The developed temporal polyrigid registration algorithm was evaluated using simulated MPI images with known motion patterns. The simulated motion patterns were chosen to represent worst-case scenarios, in the sense that the motion amplitudes between adjacent patches are close to the patch overlap. Due to the high acquisition rates of MPI, relatively small motion differences between adjacent patches are to be expected. The results of our experiments show that a motion-corrected

10.18416/ijmpi.2019.1908001

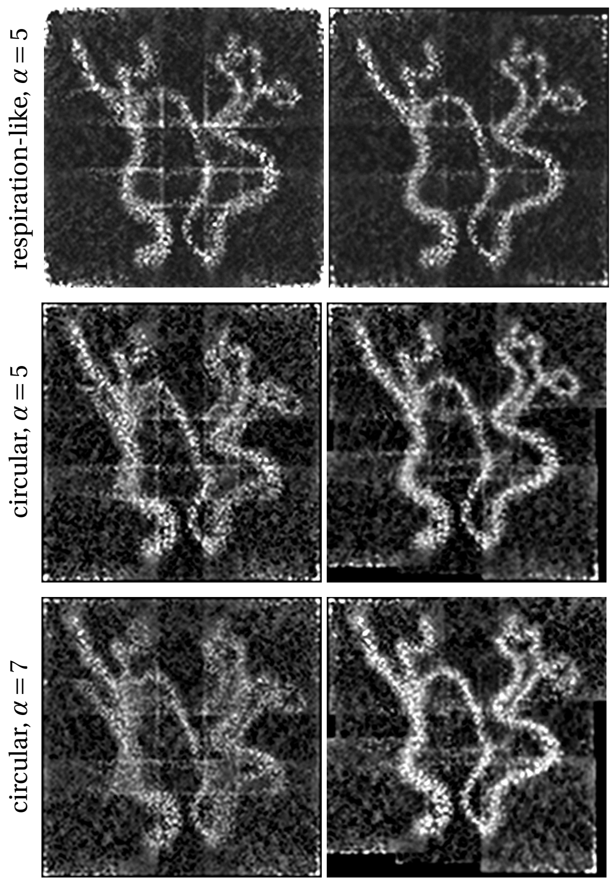

Figure 4: Registration-based reconstruction result for different simulated MPI images: reconstruction without motion compensation (left), proposed method (right).

reconstruction of patch-wise acquired MPI data in the presence of rigid object motion is possible with a high accuracy. As shown in the simulation study, images can be reconstructed successfully even in the presence of relatively large motion amplitudes, sparse image structures, low signal-to-noise ratio, and despite the presence of truncation artifacts at the patch borders (see Figure 1). The temporal smoothness constraint allows for accurate registration even if some patches share little image information due to large motion amplitudes. However, larger patch overlaps and small motion differences between adjacent patches favor registration accuracy. Our method is not based on a periodic motion assumption or repeated acquisitions as required for classical binning approaches [10, 11]. However, if a higher signal-to-noise ratio is required, the multiple acquisition of patches is already included in our approach. A restriction of the presented approach is the assumption of rigid object motion because most organ deformations related to breathing or heart beat are non-rigid. We argue that the assumption of rigid motion is approximately true if the imaged ROI is relatively small. Further, the extension of the approach to deformable object motions is possible within the same framework using spatially varying polyrigid or polyaffine transformations [16]. However, such an extension increases the number of parameters to estimate and might require larger patch overlaps.

Acknowledgements

The authors gratefully acknowledge the Federal Ministry of Education and Research, Germany (BMBF) for funding this project under Grant Nos. 13GW0071D (SKAMPI) and 01DL17010A (IMAGINE), as well as the German Research Foundation (DFG) under Grant No. BU 1436/7-1.

Author's Statement

The authors state no conflict of interest.

References

[1] B. Gleich and J. Weizenecker. Tomographic imaging using the nonlinear response of magnetic particles. *Nature*, 435(7046):1214–1217, 2005, doi:10.1038/nature03808.

[2] A. C. Bakenecker, M. Ahlborg, C. Debbeler, C. Kaethner, T. M. Buzug, and K. Lüdtke-Buzug. Magnetic particle imaging in vascular medicine. *Innovative Surgical Sciences*, 3(3):179–192, 2018, doi:10.1515/iss-2018-2026.

[3] E. U. Saritas, P. W. Goodwill, G. Z. Zhang, and S. M. Conolly. Magnetostimulation Limits in Magnetic Particle Imaging. *IEEE Transactions on Medical Imaging*, 32(9):1600–1610, 2013, doi:10.1109/TMI.2013.2260764.

[4] J. Rahmer, B. Gleich, C. Bontus, I. Schmale, J. D. Schmidt, J. Kanzenbach, O. Woywode, J. Weizenecker, and J. Borgert, Results on Rapid 3D Magnetic Particle Imaging with a Large Field of View, in *International Society for Magnetic Resonance in Medicine 19*, 629, 2011.

[5] P. Vogel, T. Kampf, M. A. Rückert, and V. C. Behr. Flexible and Dynamic Patch Reconstruction for Traveling Wave Magnetic Particle Imaging. *International Journal on Magnetic Particle Imaging*, 2(2), 2016, doi:10.18416/IJMPI.2016.1611001.

[6] M. Ahlborg, C. Kaethner, T. Knopp, P. Szwargulski, and T. M. Buzug. Using data redundancy gained by patch overlaps to reduce truncation artifacts in magnetic particle imaging. *Physics in Medicine and Biology*, 61(12):4583–4598, 2016, doi:10.1088/0031-9155/61/12/4583.

[7] C. Jung, J. Salamon, P. Szwargulski, N. Gdaniec, M. Hofmann, M. G. Kaul, G. Adam, S. J. Kemp, M. Ferguson, A. P. Khandhar, K. M. Krishnan, T. Knopp, and H. Ittrich, Using a Long Circulating Blood Pool Tracer to Perform Multi-patch MPI for Whole Body Imaging of a Mice, in *Radiological Society of North America*, 2016.

[8] R. Szeliski. Image Alignment and Stitching: A Tutorial. *Foundations and Trends® in Computer Graphics and Vision*, 2(1):1–104, 2006, doi:10.1561/0600000009.

[9] T. Vercauteren, A. Perchant, G. Malandain, X. Pennec, and N. Ayache. Robust mosaicing with correction of motion distortions and tissue deformations for in vivo fibered microscopy. *Medical Image Analysis*, 10(5):673–692, 2006, doi:10.1016/j.media.2006.06.006.

[10] T. Pan, Helical 4D CT and Comparison with Cine 4D CT, in *4D Modeling and Estimation of Respiratory Motion for Radiation Therapy*, J. Ehrhardt and C. Lorenz, Eds., 2013, 25–41. doi:10.1007/978-3-642-36441-9_2.

[11] N. Gdaniec, M. Schluter, M. Moddel, M. G. Kaul, K. M. Krishnan, A. Schlaefer, and T. Knopp. Detection and Compensation of Periodic Motion in Magnetic Particle Imaging. *IEEE Transactions on Medical Imaging*, 36(7):1511–1521, 2017, doi:10.1109/TMI.2017.2666740.

[12] N. Gdaniec, P. Szwargulski, M. Möddel, M. Boberg, and T. Knopp, Multi–patch magnetic particle imaging of a phantom with periodic motion, in *International Workshop on Magnetic Particle Imaging*, 27–28, 2019.

[13] J. Ehrhardt, R. Werner, D. Säring, T. Frenzel, W. Lu, D. Low, and H. Handels. An optical flow based method for improved reconstruction of 4D CT data sets acquired during free breathing. *Medical Physics*, 34(2):711–721, 2007, doi:10.1118/1.2431245.

[14] M. Usman, D. Atkinson, F. Odille, C. Kolbitsch, G. Vaillant, T. Schaeffter, P. G. Batchelor, and C. Prieto. Motion corrected compressed sensing for free-breathing dynamic cardiac MRI. *Magnetic Resonance in Medicine*, 70(2):504–516, 2013, doi:10.1002/mrm.24463.

[15] C. Forman, D. Piccini, R. Grimm, J. Hutter, J. Hornegger, and M. O. Zenge. Reduction of respiratory motion artifacts for free-breathing whole-heart coronary MRA by weighted iterative reconstruction. *Magnetic Resonance in Medicine*, 73(5):1885–1895, 2015, doi:10.1002/mrm.25321.

[16] V. Arsigny, O. Commowick, N. Ayache, and X. Pennec. A Fast and Log-Euclidean Polyaffine Framework for Locally Linear Registration. *Journal of Mathematical Imaging and Vision*, 33(2):222–238, 2009, doi:10.1007/s10851-008-0135-9.

[17] C. Seiler, X. Pennec, and M. Reyes, Simultaneous Multiscale Polyaffine Registration by Incorporating Deformation Statistics, in *Medical Image Computing and Computer-Assisted Intervention*, 130–137, 2012. doi:10.1007/978-3-642-33418-4_17.

[18] P. Cachier, E. Bardinet, D. Dormont, X. Pennec, and N. Ayache. Iconic feature based nonrigid registration: the PASHA algorithm. *Computer Vision and Image Understanding*, 89(2-3):272–298, 2003, doi:10.1016/S1077-3142(03)00002-X.

[19] J. Ehrhardt, M. Ahlborg, H. Uzunova, T. M. Buzug, and H. Handels, Temporal polyrigid registration for patch-based MPI reconstruction of moving objects, in *International Workshop on Magnetic Particle Imaging*, 55–56, 2018.

[20] K. McLeod, C. Seiler, M. Sermesant, and X. Pennec, A Near-Incompressible Poly-affine Motion Model for Cardiac Function Analysis, in *Statistical Atlases and Computational Models of the Heart. Imaging and Modelling Challenges*, 2013, 288–297. doi:10.1007/978-3-642-36961-2_33.

[21] C. Seiler, X. Pennec, and M. Reyes. Capturing the multiscale anatomical shape variability with polyaffine transformation trees. *Medical Image Analysis*, 16(7):1371–1384, 2012, doi:10.1016/j.media.2012.05.011.

[22] V. Arsigny, X. Pennec, and N. Ayache. Polyrigid and polyaffine transformations: A novel geometrical tool to deal with nonrigid deformations – Application to the registration of histological slices. *Medical Image Analysis*, 9(6):507–523, 2005, doi:10.1016/j.media.2005.04.001.

[23] L. Le Folgoc, H. Delingette, A. Criminisi, and N. Ayache. Sparse Bayesian registration of medical images for self-tuning of parameters and spatially adaptive parametrization of displacements. *Medical Image Analysis*, 36:79–97, 2017, doi:10.1016/j.media.2016.09.008.

[24] J. Ehrhardt and C. Lorenz, Eds., 4D Modeling and Estimation of Respiratory Motion for Radiation Therapy, ser. Biological and Medical Physics, Biomedical Engineering. Berlin, Heidelberg: Springer Berlin Heidelberg, 2013, doi:10.1007/978-3-642-36441-9.

10.18416/ijmpi.2019.1908001